



Effects of nanosized precipitates on irradiation behavior of CoCrFeNi high entropy alloys

P.P. Cao^a, H. Wang^{a,*}, J.Y. He^b, C. Xu^c, S.H. Jiang^a, J.L. Du^c, X.Z. Cao^d, E.G. Fu^{c,*}, Z.P. Lu^a

^a Beijing Advanced Innovation Center for Materials Genome Engineering, State Key Laboratory for Advanced Metals and Materials, University of Science and Technology Beijing, Beijing 100083, China

^b Department of Microstructure Physics and Alloy Design, Max-Planck-Institut für Eisenforschung GmbH, Max-Planck-Straße 1, D-40237 Düsseldorf, Germany

^c State Key Laboratory of Nuclear Physics and Technology, School of Physics, Peking University, Beijing, China

^d Key Laboratory of Nuclear Analysis Techniques, Institute of High Energy Physics, Chinese Academy of Sciences, Beijing 100049, China



ARTICLE INFO

Article history:

Received 3 September 2020

Received in revised form 7 December 2020

Accepted 9 December 2020

Available online 13 December 2020

Keywords:

High entropy alloy

Ion irradiation

Precipitates

Irradiation hardening

ABSTRACT

Evolution of nanosized precipitates in typical $(\text{CoCrFeNi})_{94}\text{Ti}_2\text{Al}_4$ high entropy alloys under irradiation and its effect on the irradiation resistance were investigated in detail. The as-solutionized samples and the aged samples with massive nanosized precipitates were irradiated at ambient temperatures with a dose ranging from 10 to 49 dpa of 4 MeV Au ions. It was found that the ordered precipitates became disordered quickly at the early stage under 10 dpa irradiation, accompanying with the dissolution process which became more and more severer at higher doses. After irradiation, the hardness slightly changed in the aged specimens containing massive precipitates, but increased by > 30% in the as-solutionized ones with no precipitates. The obvious hardness increment in the as-solutionized samples is due to the creation of defects while the small variations of the hardness in the aged specimens can be ascribed to the disordering and dissolution of precipitates. In addition, the size of dislocation loops induced by the irradiation in the aged specimens is much smaller than that in the as-solutionized samples. We confirmed that presence of the nanosized precipitates delayed defect evolution and reduced the sizes of dislocation loops.

© 2020 Elsevier B.V. All rights reserved.

1. Introduction

High entropy alloys (HEAs) constitute a new family of metallic materials containing four or more principle elements at equimolar or near-equimolar ratios, which generally form simple solid solution phases, instead of complex microstructures with many intermetallic compounds [1,2]. HEAs have been reported to possess a unique combination of decent mechanical properties, such as high strength, high hardness, improved wear resistance, good corrosion and oxidation resistance [3–8]. Recently, HEAs were found to have promising irradiation resistance [9–16]; For example, the CrFeMnNi HEA exhibits better irradiation resistance than conventional austenitic alloys under Ni ion irradiation at elevated temperatures (400–700 °C) [9], and the defect growth in the CoCrFeNi HEA was found to be > 40 times slower than in pure Ni [10]. Prompt research activities were devoted to revealing the underlying mechanism; Zhang et al. unveiled that chemistry complexity of HEAs could suppress damage accumulation during irradiation, which attributed

to slow energy dissipation [11], whereas Lu et al. found that the compositional complexity could also reduce defect mobility and alter migration paths on a modified energy landscape to make irradiation damage annihilate [12]. Detailed studies of HfNbZr and CoCrCuFeNi alloys, coupled with computer simulations, uncovered that the high atomic-level stresses in HEAs lead to the possibility of achieving irradiation damage healing by crystal-amorphous-crystal process [13,14]. All these preliminary studies mentioned above indicate that HEAs have great potential to be utilized as high irradiation tolerant materials due to their unique properties, viz., compositional complexity and large lattice distortion.

Superior mechanical properties are essential requirement for nuclear materials, and precipitation hardening is a key approach to enhancing materials properties. Recently, several attempts focusing on precipitation hardening in HEAs have been reported [17–20]. For example, minor addition of Ti and Al into the CoCrFeNi HEA results in the formation of L1₂ coherent nanosized precipitates, which significantly enhances the strength of the alloy but maintains decent plasticity simultaneously [17]. Obviously, evolution of precipitates and its consequent impact on the materials are crucial for nuclear applications. In traditional alloy systems, the dissolution, coarsening,

* Corresponding authors.

E-mail addresses: wanghui@ustb.edu.cn (H. Wang), efu@pku.edu.cn (E.G. Fu).

amorphization and redistribution of the precipitates during irradiation have been comprehensively reported [21–24]. For highly concentrated solid-solution HEAs, stability of precipitates under high-temperature ion irradiation was studied in several systems, such as FeCoNiCrTi0.2 alloy [25] and Al0.3CoCrFeNi alloy [26]. However, evolution of precipitates in HEAs under room-temperature irradiation and its effects on the mechanical performance have not been investigated yet.

In this study, we evaluated effects of the nanosized precipitates in HEAs subjected to irradiation. Owing to its large number of fine precipitates and desirable mechanical properties [17], the CoCrFeNi HEA doped with 2 at% Ti and 4 at% Al, i.e., $(\text{CoCrFeNi})_{94}\text{Ti}_2\text{Al}_4$ (at%), was selected as our model material. Focuses were placed on the microstructure and hardness changes after Au ion irradiation so that evolution of precipitates and its effects on the radiation damage resistance can be revealed.

2. Experimental

Ingots with a nominal composition of $(\text{CoCrFeNi})_{94}\text{Ti}_2\text{Al}_4$ (at%) were prepared by vacuum arc melting, and the details about alloy preparation and thermomechanical treatment can be found in our previous publication [17]. Each alloy ingot was melted at least eight times to ensure homogenous mixing before drop-casting into a copper mold. The as-cast bars were homogenized at 1200 °C for 4 h (hereafter refer to as alloy A) and then cold rolled and recrystallized at 800 °C for 18 h (i.e., alloy B). Microstructure characterization was performed with a Zeiss Supra 55 scanning electron microscope (SEM) and a Tecnai F30 transmission electron microscope (TEM) operated at 300 kV. The size and volume fraction of nanosized precipitates were measured by commercial image-analysis software (Image Pro Plus 6.0). All measurements were made from the dark field images taken from the ordered L_1_2 superlattice reflection. More than 1000 precipitates were measured by Image Pro Plus to achieve a statistically reliable analysis.

The irradiation experiment was performed at a 2x1.7 MV tandem accelerator of Electron Microscopy Laboratory of Peking University. Before being irradiated, specimens were polished to 2000-grit SiC paper and then electropolished by using 10% perchloric acid and 90% ethanol. Both alloys were implanted with 4 MeV Au ions to three different fluences of 2×10^{15} , 5×10^{15} and 1×10^{16} ion/cm² at room temperature.

The irradiation damage level was computed by SRIM 2013 with both the quick Kinchin-Pease mode [27] and full-cascade modes [28]. The threshold displacement energy of the metals is 40 eV and the depth profiles of atomic displacement damage calculated by the two methods are plotted in Fig. 1. As can be seen, both approaches show similar atomic displacement profiles at each dose, although the displacement damage estimated from the full-cascade mode is consistently higher. In this study, the SRIM quick Kinchin-Pease damage calculation was used to estimate the damage level due to the availability of more data in conventional irradiated alloys. The calculated maximum implantation depth of Au ions is 600 nm distance from the ion incident surface and the maximum damage doses reach 10, 25 and 49 displacements per atom (dpa).

Cross-sectional TEM samples from the irradiated specimens were prepared by focus ion beam (FIB). Scanning transmission electron microscopy (STEM) equipped with energy dispersion spectrum (EDS) was used to identify the chemical distribution of precipitates under irradiation. Grazing incidence X-ray diffraction (GIXRD) was carried out at Rigaku D_{max}-RB equipment with Cu K α radiation. The incidence angle is 0.4° and the depth of penetration is 360 nm. The scanning step size is 0.02° with a time interval of 1 s per step.

The nanoindentation hardness tests were conducted on a MTS DSM nanoindentation. The continuous stiffness measurement (CSM) mode was chosen to determine hardness versus depth profiles of the

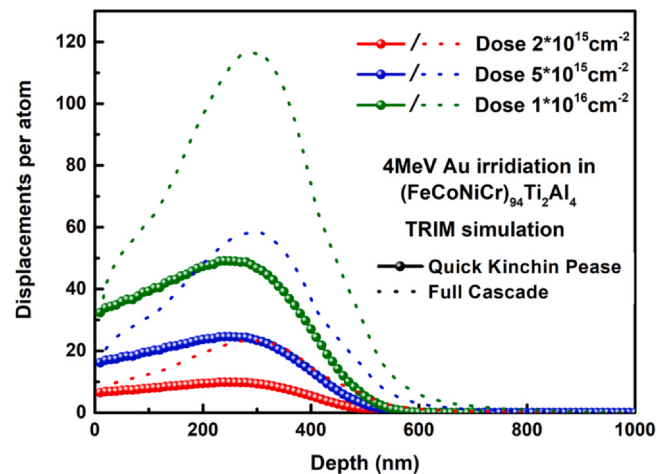


Fig. 1. Depth distribution of dpa calculated by SRIM in $(\text{FeCoNiCr})_{94}\text{Ti}_2\text{Al}_4$ irradiated with 4 MeV Au ions. Sphere symbols represent the damage distribution computed by quick Kinchin-Pease mode while the dotted curves represent that by full cascade mode.

specimens. To obtain an average hardness, each specimen was indented 20 points with the distance of 50 μm . The slow positron annihilation technique (SPAT) experiment was conducted at the institute of High Energy Physics, Chinese Academy of Sciences. Doppler broaden energy spectrum of positron annihilation measurements were performed on the as-prepared specimens and room temperature irradiated specimens. S-parameter and W-parameter, which could represent positron annihilation information, characterized the evolution of defect concentration and defect types, respectively.

3. Results

3.1. Microstructures of unirradiated alloys

Microstructure of A and alloy B is shown in Fig. 2a and b, respectively. Clearly, alloy A has a single fcc (face-centered-cubic) structure, which can be further confirmed by its XRD pattern shown in Fig. 2d. Nevertheless, a significant amount of fine precipitates was found in alloy B, as vividly demonstrated by a high magnification SEM image in Fig. 2c.

TEM bright field and dark field images of alloy B show a uniform distribution of nanosized, spherical precipitates in the matrix. The size and the volume fraction of the particles were estimated to be about 20 nm and 35%, respectively. The EDS mapping of the unirradiated sample was performed and the results are shown in Fig. 3c-h. It is found that the precipitates are enriched with Ni, Al, Ti while the fcc matrix has a higher amount of Fe, Cr and Co. The interfaces between the matrix and precipitates are clearly visible in the EDS images. The corresponding selected area electron diffraction (SAED) patterns taken along different axes show three sets of diffraction spots, indicating that the structural relationship between the fcc matrix and precipitates is coherent. Weak spots originate from the γ' precipitates marked by blue font, implying a chemically ordered L_1_2 structure, which is consistent with our previous results [17]. Noted that the reflection peaks of these precipitates were not detected on the XRD trace, which might be due to their small sizes.

3.2. Microstructure of irradiated alloys

GIXRD experiments were performed on both the as-prepared and room-temperature irradiated samples to reveal structure stability of $(\text{CoCrFeNi})_{94}\text{Ti}_2\text{Al}_4$ against irradiation, and the corresponding results are

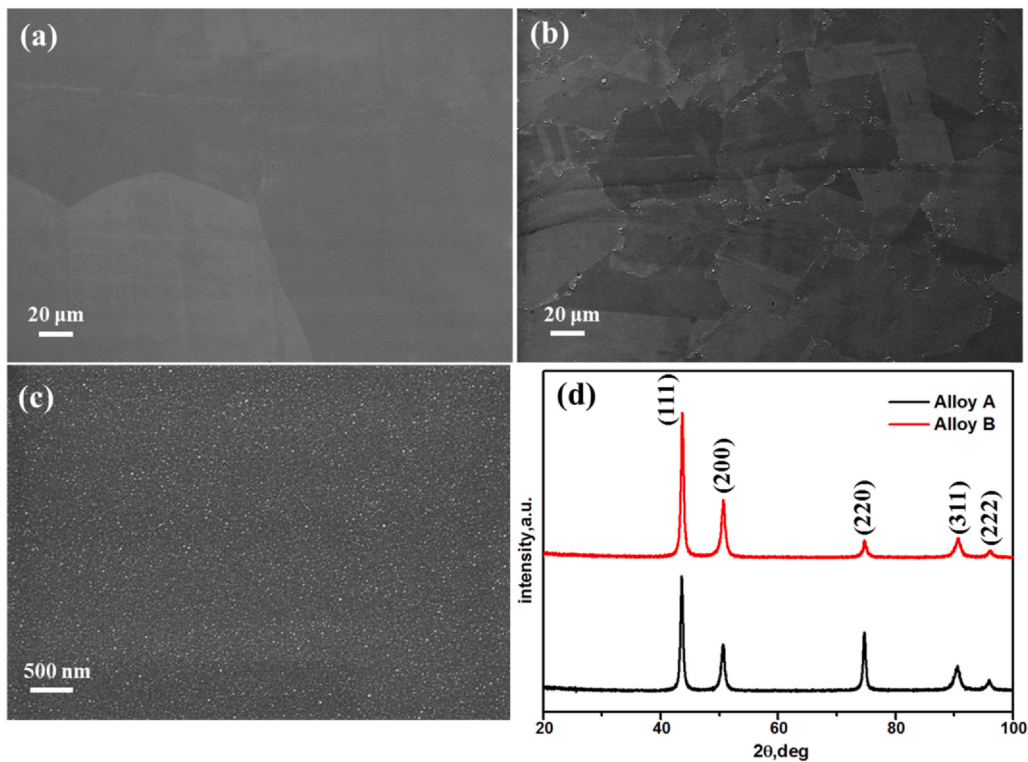


Fig. 2. SEM images of the as-prepared alloy A (a) and alloy B (b, c). XRD trace (d) shows that the as-prepared alloy A and alloy B are both fcc single phases.

shown in Fig. 4a and b, respectively. For all the samples, five crystalline peaks corresponding to the fcc reflections of the (111), (200), (220), (311) and (222) planes, respectively, are presented. These observations

clearly confirm that there is no new phase formed in both alloys A and B when being subjected to 10, 25 and 49 dpa irradiation at room temperature.

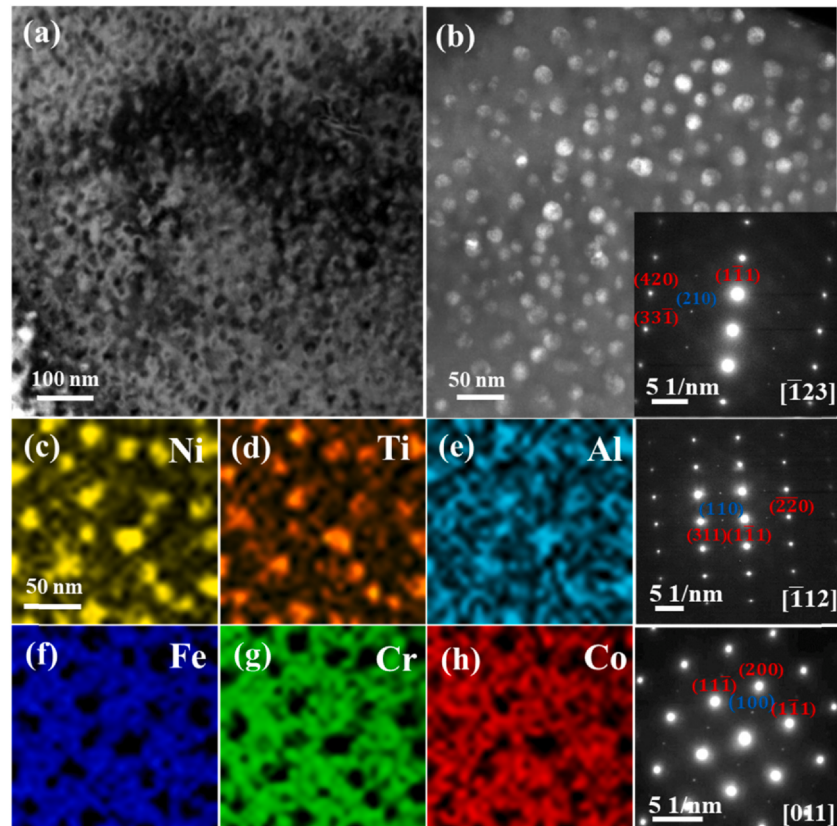


Fig. 3. Bright field (a) and dark field (b) TEM images of the as-prepared alloy B and the corresponding elemental-distribution maps obtained by STEM-EDS (c-h).

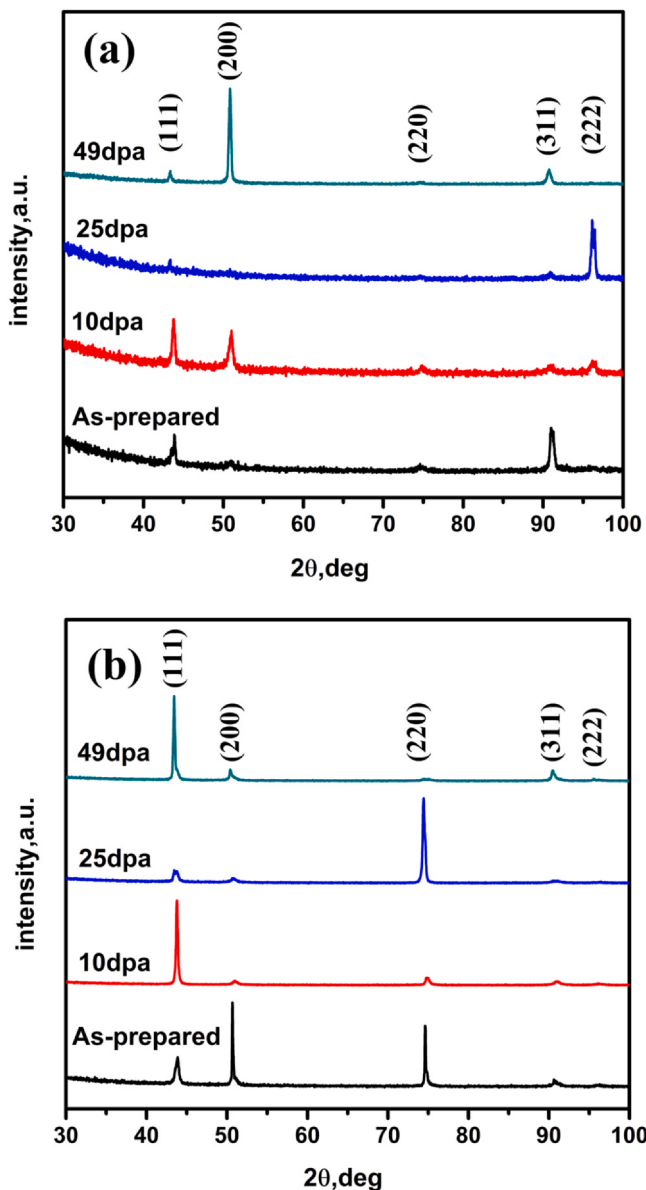


Fig. 4. GI-XRD patterns of the as-prepared and irradiated alloy A (a) and alloy B (b) exposed to different doses of Au ions.

To further understand the precipitates evolution in the irradiated materials, EDS elemental mapping from the surface to depth of 150–400 nm was conducted and the SAED patterns under the [112] zone axis was taken for the irradiated alloy B. From the diffraction patterns in the rightmost panel of Fig. 5, we can see that there is only one set of diffraction spots remaining in the irradiated region, and the secondary phase diffraction spots disappeared in all the irradiated samples.

According to the method proposed by Carpenter et al., the degree of long range order parameter S can be estimated by the expression $S \sim \sqrt{I_s/I_f}$, where I_s and I_f are the intensity of the superlattice and fundamental reflections, respectively [29]. The decrease in the intensity of the superlattice reflections indicates that the degree of order in the specimen decreases. Therefore, the disappearance of the weak spots indicates that complete disordering of the precipitates occurred, namely, the ordered L1₂ structure of precipitates was destroyed during the room-temperature ion irradiation.

The chemistry change in the precipitates under irradiation was revealed also by the EDS images, and the results are shown in Fig. 5.

As can be seen, the size of the precipitates in the 10 dpa irradiated alloy B is almost unchanged, as compared with that of the as-prepared state. Nevertheless, the boundaries of precipitates are no longer clear but became somewhat fuzzy, indicating the occurrence of early dissolution. Interestingly, the enrichment of Ni and Ti in the precipitates is still strong but the segregation of Al is mitigated. The edges of precipitates cannot be clearly distinguished in the Al-EDS image. With the increase of doses, the interfaces between the matrix and precipitates become pretty rough and the shape of precipitates is no longer spherical at the 25 dpa dose, and partial dissolution of the precipitates even occurred at 49 dpa. Obviously, the segregation of Ni, Ti and Al elements in precipitates decreases with the increase of irradiation dose. In the 49 dpa irradiated alloy B, the core of the precipitates is still enriched with Ni and Ti, but the concentration of Ni and Ti at the peripheral region of the precipitates is much lower. Moreover, Al distributed uniformly in the matrix. The difference in the dissolution behavior of these three elements is due to their different atomic mass. Compared with Ni and Ti, the relatively smaller atomic mass of Al makes it displaceable over a longer distance after the ballistic collision with ions. It can be conjectured that the precipitates will completely dissolve into the matrix under protracted irradiation.

To reveal the defect configuration in these irradiated materials, TEM characterization was also conducted on the two 10 dpa irradiated alloys. In both alloy A and B specimens, no void formation was observed in the TEM images. Generally, the void formation is greatly dependent on the elevated irradiation temperature. The current room-temperature radiation study aims to reveal influence of ion implantation on stability of the precipitates by eliminating temperature, and as such, the microstructural change under irradiation, i.e., the evolution of dislocation loops, can be properly understood. Fig. 6a and b display the bright field (BF) images of these specimens taken under the two-beam condition. The dislocation loops were observed in both irradiated alloys A and B, but their size distribution and density are different, as clearly shown in Fig. 6c. The dislocation loop sizes were measured by the longest axis of visible loops from the BF images. In alloy A, the size of dislocation loops varies greatly, and the largest dislocation loop exceeds 100 nm, but in alloy B, the maximum dislocation loop size is only 26 nm and the variation of the dislocation loop sizes is relatively small. Meanwhile, compared with alloy A, a slight increase in area dislocation loop density in alloy B was observed.

3.3. Nanoindentation tests

Fig. 7a and b shows the nanoindentation hardness profiles of alloys A and B before and after irradiation. We ignored the hardness data with indentation depth $h < 100$ nm due to reverse indentation size effect [30]. When $h > 100$ nm, the hardness decreases with the increase of indent depth, which is called as the indentation size effect (ISE). Nix and Gao developed a model based on a concept of geometrically necessary dislocation to explain the normal indentation size effect [31]. Based on the Nix-Gao model, the hardness depth profile can be given by the following equation:

$$H^2 = H_0^2(1 + (h^*/h)) \quad (1)$$

where H is the hardness at the depth of h , H_0 is the hardness at infinite depth (i.e., bulk-equivalent hardness) and h^* is a characteristic length that depends on the material and the indenter shape. The value of H_0 excludes the size effect, which is usually considered to characterize the hardening effect of irradiated alloys. The hardness data are then replotted as H^2 verse $1/h$, as shown in Fig. 7c and d. In addition, the bulk equivalent hardness values H_0 obtained based on the Nix-Gao model is also shown in Fig. 7e.

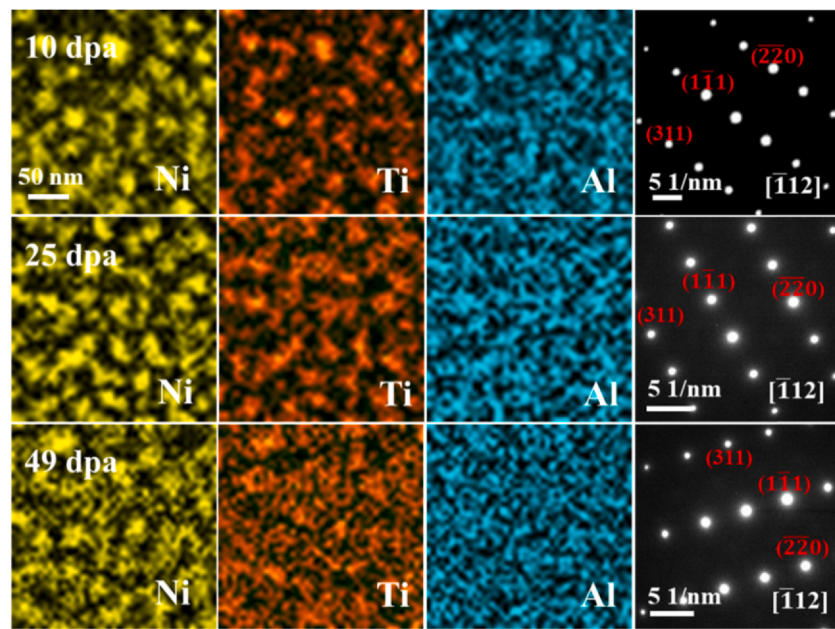


Fig. 5. Post-irradiation STEM mapping at 150–400 nm depth of alloy B. The last column showing selected area diffraction patterns at irradiated regions.

For the as-prepared alloys A and B, the hardness data both show good linearity in the range of $h > 100$ nm. The value of H_0 of alloy A and B, which can be calculated from the least square fitting of the hardness data according to Eq. (1), is 2.81 and 3.92 GPa, respectively. Alloy B is harder than of alloy A, which is apparently due to the precipitation hardening effect resulted from the enormous amount of fine precipitates presented in its matrix. After irradiation, however, both types of alloys clearly show a bi-linearity with a shoulder at 300 nm. This phenomenon is contributed by softer unirradiated region (substrate) underneath the harder ion-irradiated surface. As reported, the measured hardness value H is affected by the region extending to about 5–7 times of h [32]. Due to existence of the soft substrate in the irradiated samples, the bulk-equivalent hardness of ion-irradiated materials can only be obtained from the shallower depth region before the shoulder by excluding “the soft substrate effect” [33].

After irradiation, the hardness of alloy A increases, nevertheless, the value hovers around 3.72–3.85 GPa for the specimens irradiated with a different dose of 10, 25 and 49 dpa, indicating that the irradiation hardening in alloy A saturates with the dose of 10 dpa. Similar saturation of irradiation hardening was also observed in the other traditional materials such as stainless steels [34]. For alloy B, however, the irradiated samples show no shoulder at around 300 nm. Moreover, the hardness values first increased from 3.92 to 4.27 GPa after irradiation to 10 dpa, then decreased to 4.05 GPa after 25 dpa, and eventually decreased to 3.95 GPa for the dose of 49 dpa, a value close to that of the as-prepared alloy B. For better comparison, the hardness increment was normalized with that of the as-prepared specimens, and the results are shown in Fig. 7e. Compared with its as-prepared condition, the hardness of alloy A increases above 30% under three different irradiation doses, but that of alloy B under similar irradiation conditions changed inappreciably.

3.4. Slow positron annihilation measurements

To understand the aforementioned irradiation behavior, slow positron annihilation experiments were conducted. Fig. 8 shows the Doppler S-parameter as a function of positron beam energy (i.e., the mean implantation depth) and the S-W plots for the as-prepared and irradiated samples with different doses. It is well known that

vacancy-like defects induced by irradiation tend to increase the S-parameter [35,36]. For the as-prepared alloy A, the S-parameter is high at the surface, then decreases with the implantation depth and finally stabilizes at 0.42 with the positron energy of 8 keV. High values of the S-parameter at low positron energy, which is attributed to positron annihilation at the surface, is a typical phenomenon in the S-E profiles. Therefore, the data below 8 keV positron energy can be neglected because of the surface effect, and so can the data of the Doppler profiles. The S-parameter values for the irradiated samples become larger, as compared with those for the as-prepared sample, indicating that vacancy-like defects generated during irradiation. Similar phenomena have been reported in CoCrFeNi HEAs irradiated with low doses at room temperature [35]. The S-parameter values have no change when the samples exposed to the higher Au-ion irradiated doses, revealing that the vacancy type defects induced by irradiation saturates at 10 dpa or even lower. Similarly, the S-parameter values of alloy B after irradiation with different doses all increased by 0.04, which is the same as that in alloy A. These observations suggest that the Au ion irradiation produced a certain degree of vacancy-related defects in both alloys A and B, and the defects have approached an upper limit at 10 dpa. Usually, the S-W plots are used to describe the type of defects created by ion irradiation of the alloys. Fig. 8c and d shows the comparison of the S-W plots between the as-prepared and irradiated alloys, and the arrows represent the increasing positron implantation energy. It is clearly seen that the S-W plots for the as-prepared alloys A and B can be both fitted by one straight line, which indicates that only one type of defect (open volume type of defects) exists in the as-prepared samples. Nevertheless, some other types of defects also present after irradiation, as evidenced by the nonlinearity of the S-W data points for the irradiated samples [37,38].

4. Discussion

It is generally accepted that the irradiation hardening behavior is due to the defects (i.e. dislocation loops, clusters and voids etc.) induced by ion implantation. For the 10 dpa-irradiated alloy A, the enhanced hardness is partially because of massive dislocation loops, as revealed by TEM shown in Fig. 6a. With further irradiation, the hardening effect stabilize around 34%, indicating saturation in the

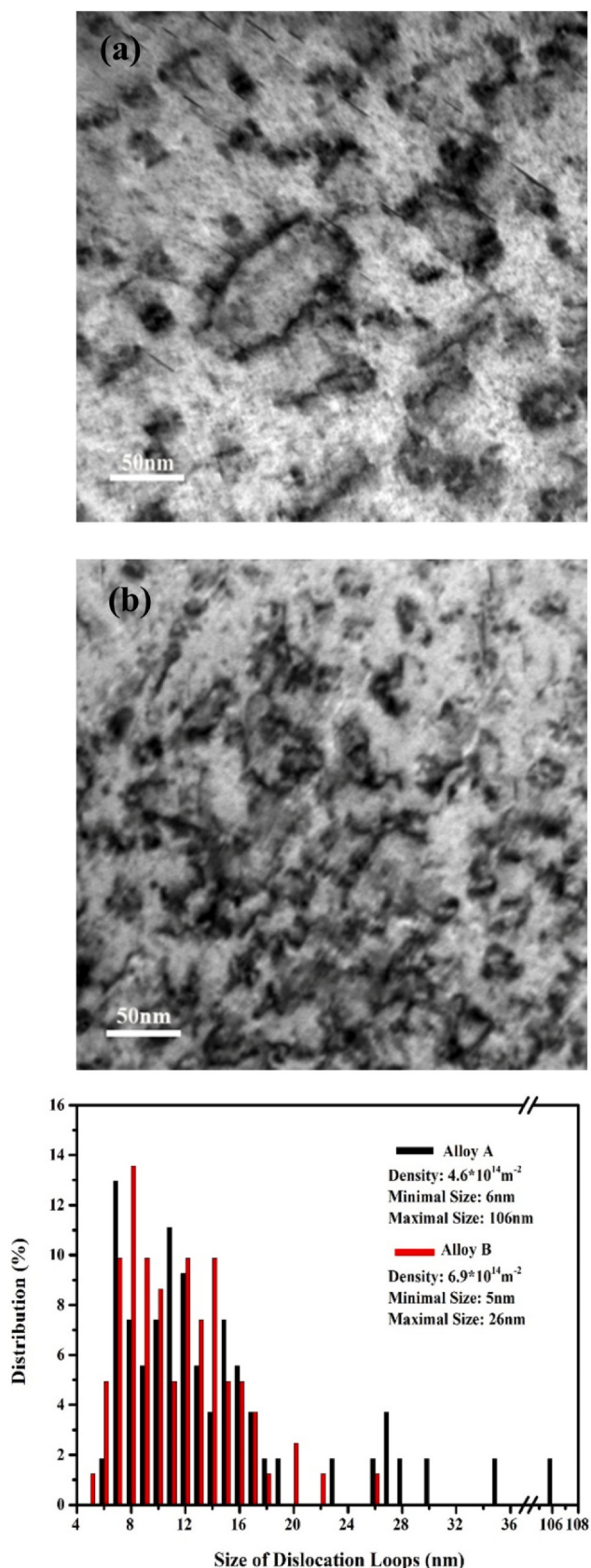


Fig. 6. Two beam condition TEM images of irradiated alloy A (a) and alloy B (b), and the size distribution of dislocation loops (c) after 10 dpa irradiation.

creation of defects. Among these defects induced by irradiation, the vacancy type defects detected by SPAT are already in a state of saturation at 10 dpa, which is consistent with the above nanoindentation conclusion. According to Huang et al., the hardness of nickel-based GH3535 alloy increases by 44% when irradiated with Xe ions to a dose of 10 dpa at room temperature [39], whilst that of pure Ni and Ni-35Fe irradiated by Ni ions to 6.5 dpa dose at room temperature is increase by 200% and 50%, respectively [40]. Clearly, the current HEAs exhibit larger resistance to irradiation-induced hardening than not only pure Ni and the Ni-35Fe alloy [39], but also the GH3535 alloy, which is a newly developed irradiation tolerant nickel-based alloy with promising irradiation tolerance [39]. It was previously reported that the defect cluster motion of a short-range three-dimensional mode in HEAs and the similar mobility of vacancies and interstitials in most equiatomic fcc HEAs will magnify recombination of defects under irradiation, which will result in a reduction in defect concentration in HEAs [12]. Furthermore, the chemical complexity in HEAs are found to be propitious to decrease electrical and thermal conductivities, and this slow energy dissipation may lead to the promotion of defect recombination [11]. Therefore, the unique properties of HEAs (e.g., the local lattice distortion and the chemistry complexity) determine the recombination of point defects in irradiated samples. Coincidentally, the low hardening rate of alloys A and B verifies the low concentration of point defects under irradiation and the enhanced irradiation tolerance of HEAs.

However, for alloy B, no significant hardening was found after all the three different doses irradiation. Based on the dark field image and the STEM maps of the irradiated alloy B, it is clear that the precipitates disordered and dissolved into the matrix due to the ion bombardment. In light of these findings, we can conclude that the insensitive change of the irradiated alloy B is resulted from the following factors: the increment of hardness induced by irradiation defects and the reduction of hardness resulted from disordering and dissolution of the precipitates. As elaborated above, the precipitates in the CoCrFeNi HEA become disordered immediately after irradiation at room temperature and dissolved into the matrix at early stage under a dose of 10 dpa. After the irradiation of 49 dpa, the precipitates are partially dissolved into the matrix. During irradiation, the evolution of precipitates is driven by two competitive processes; one is atomic ballistic mixing arising from collision cascades, leading to the disordering and dissolution of precipitates. The other is re-ordering process driven by irradiation enhanced diffusion and thermal diffusion. Vacancies induced by irradiation enhance diffusion on the premise that they are mobile [23,41]. At room temperature, the vacancies are frozen in and difficult to diffuse, the irradiation enhanced diffusion and thermal diffusion are both restricted and then recovery of disordering is limited. Accordingly, the atomic mixing is dominated and destruction of long-range ordered in precipitates is prone to happen. According to our results, the precipitates became disordered very quickly before a significant dissolution of the precipitates. This type evolution of precipitates was also experimentally observed in Nimonic PE16 irradiated with Ni ions at room temperature, and the time constants of disordering process is about two orders of magnitude larger than that of dissolution process [42]. During irradiation process, disordering reduces the ordered strengthening by destroying the antiphase boundaries in the ordered precipitates, dissolution mitigates interfacial strengthening originating from misfit strain between the precipitates and matrix [43,44]. After three doses irradiation at room temperature, the precipitates in alloy B become completely disordered, but stay in the form of solute-rich aggregates, which still contribute to the hardness. As shown in Fig. 5, the degree of

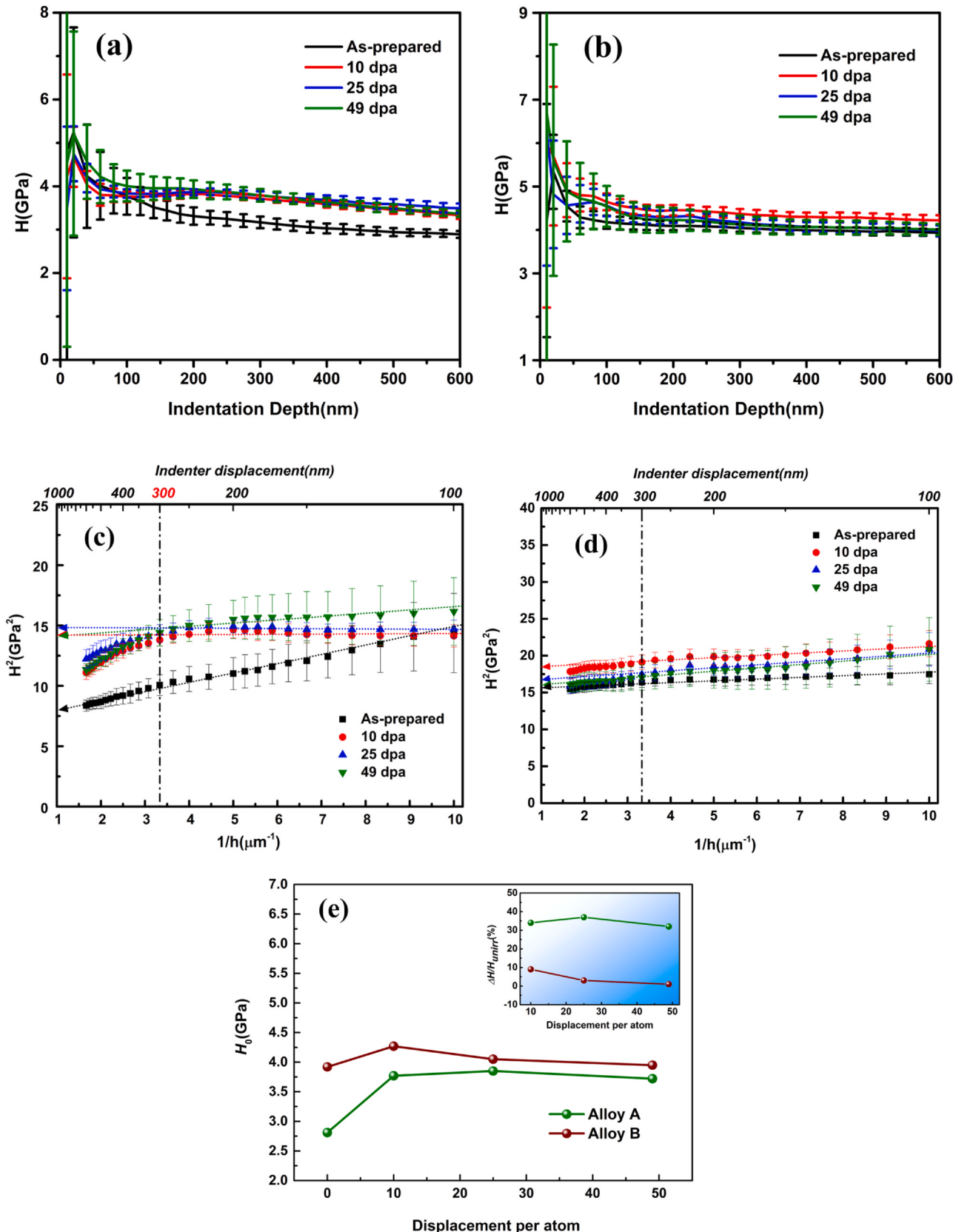


Fig. 7. Nanoindentation hardness as a function of measuring depth in the as-prepared and irradiated alloy A (a) and alloy B (b) with different doses. Curves of H^2-1/h for average nanoindentation hardness of alloy A (c) and alloy B (d). The bulk equivalent hardness values (H_0) obtained based on the Nix-Gao model, along with the irradiation hardening ($\Delta H/H_{unirr}$) of the investigated samples (e).

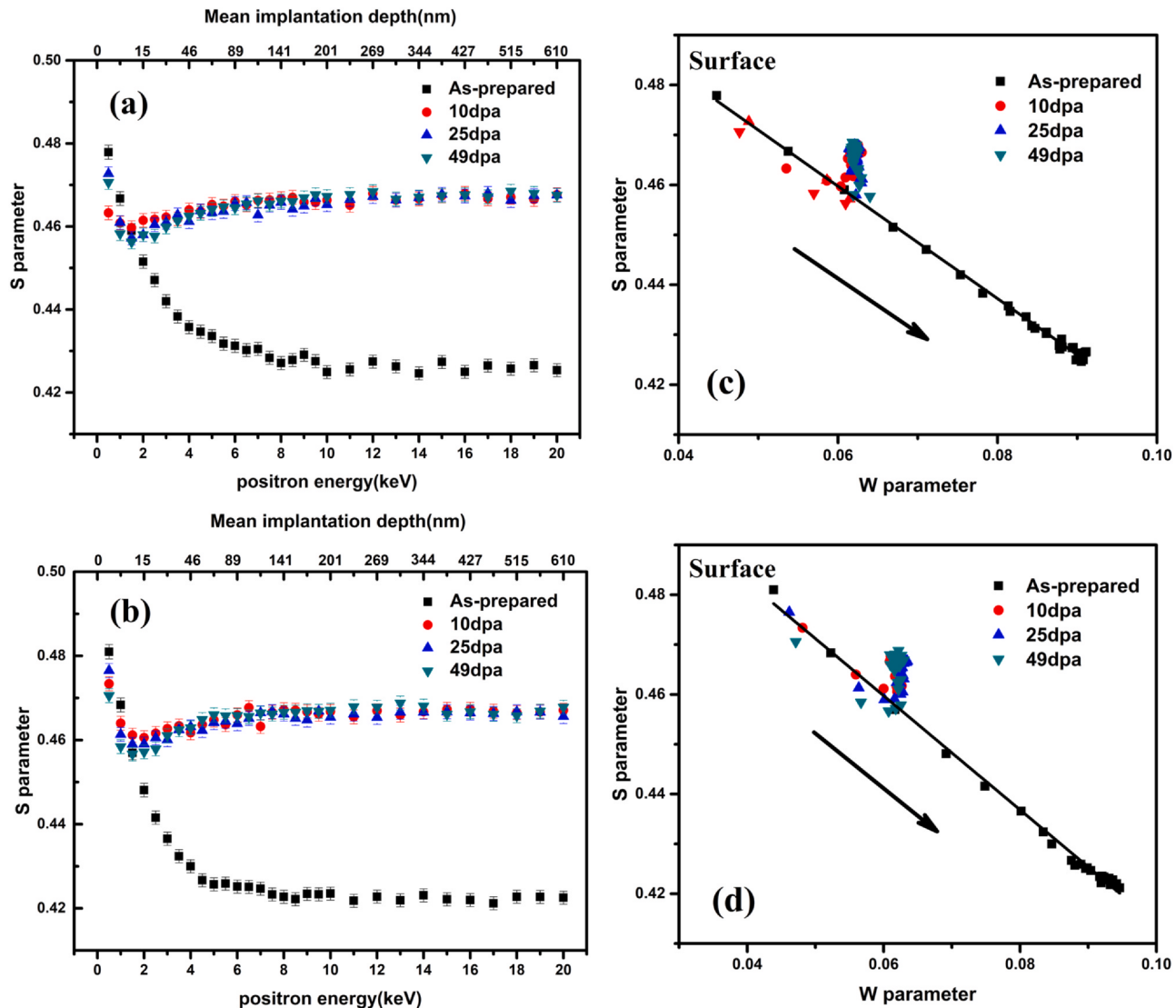


Fig. 8. S parameter as a function of incident positron energy (mean implantation depth) in the as-prepared and irradiated alloy A (a) and alloy B (b). S-W parameter plots in the as-prepared and irradiated alloy A (c) and alloy B (d).

precipitates dissolution aggravates with the increasing of irradiation dose, which leads to a decrease in the contribution of chemical aggregation on the hardness. This inference is confirmed by the smaller hardness values in the specimens irradiated with higher doses. The hardness of the specimen irradiated at 10 dpa is larger than that irradiated at 25 dpa, and the hardness of 49 dpa irradiated specimen is the smallest.

Usually, the dislocation loop evolution of materials after irradiation can be briefly divided into three stages, viz., stage I is nucleation of dislocation loops. During the preliminary stage of irradiation, the dislocation loops are formed by the collapse of vacancy-rich cores induced by the ion bombardment and the loop size and density is both small. Stage II is the growth of dislocation loops. With the irradiation dose increases, the dislocation loops grow up by absorbing the point defects and the smaller dislocation loops nearby. Therefore, the density of dislocation loops decreases at this stage. Stage III is the coalescence of dislocation loops. When the irradiation dose keeps increasing, the dislocation loops will coalesce to form the dislocation networks [45,46]. Herein, dislocation loops were observed in both alloy A and alloy B, as shown in Fig. 6. After irradiation, alloy B shows a smaller loop size on average and a higher density of dislocation loops, indicating that the growth process of

the dislocation loops in alloy B is retarded. In this regard, alloy B has a better radiation resistance than alloy A. According to previous results [17], the matrix of alloy B consists of 1.3 ± 0.1 (at%) Al, 0.8 ± 0.1 Ti, 25.8 ± 0.1 Cr, 24.4 ± 0.2 Fe, 26.1 ± 0.2 Co and 21.6 ± 0.2 Ni. The chemical composition difference of the elements in alloys A and B is less than 3 at%. Moreover, the matrices of both alloys constitute the same fcc solid solution lattice. In this case, effect of the chemical difference on the nucleation and movement of dislocations, i.e., evolution of dislocation loops, in these two matrices is secondary, as compared with that of precipitates. Note that Fan et al. [47] reported that the preferential diffusion of vacancies through Fe/Cr led to the change of chemical concentration in the irradiated NiCoFeCr HEA matrix, which in turn leads to the void evolution during irradiation. Clearly, this irradiation-driven composition fluctuation is different from our case where evolution of nanoprecipitates plays a dominant role. Although the interfaces of coherent precipitates contain limited defect sites, several previous studies still reported that the nanoscale coherent precipitates could efficiently remove vacancies under irradiation [48,49]. It was argued that accumulation of point defects with coherent precipitates is not the result of defects being trapped at the interfaces, but rather restricted flow of defects as they pass through the interfaces [50]. Therefore,

we infer that the nanoscale precipitates are responsible for the delay of the dislocation loop evolution.

5. Conclusions

In summary, evolution and influences of nanosized precipitates in fcc CoCrFeNi HEAs during irradiation were studied. Two kinds of HEAs (i.e., single phased alloy A and alloy B with massive nanosized precipitates) were irradiated with 4 MeV Au ions at room temperature. It was found that these HEAs both exhibit good phase stability with no new phase formed. Meanwhile, the two kinds of alloys produced a certain degree of vacancy-related defects and have been in a state of saturation at 10 dpa irradiation dose. Moreover, the growth of dislocation loops in alloy B is appreciably smaller than that in alloy A, confirming that existence of the numerous nanosized precipitates can retard defects evolution during irradiation. Furthermore, alloy B exhibits a negligible effect on hardness, whilst alloy A produces above 30% hardening under the same irradiation condition. The disordering and partial dissolution of the precipitates observed in alloy B was found to be responsible for the low irradiation hardening.

CRediT authorship contribution statement

P.P. Cao: Methodology, Data curation, Writing - original draft, Writing - review & editing. **H. Wang:** Data curation, Writing - review & editing. **J.Y. He:** Data curation, Supervision. **C. Xu:** Investigation. **S.H. Jiang:** Methodology, Data curation. **J.L. Du:** Methodology. **X.Z. Cao:** Investigation. **E.G. Fu:** Data curation, Supervision, Writing - review & editing. **Z.P. Lu:** Data curation, Supervision, Writing - review & editing.

Declaration of Competing Interest

The authors declare that they have no known competing financial interests or personal relationships that could have appeared to influence the work reported in this paper.

Acknowledgments

This research is supported by National Natural Science Foundation of China (Nos. 51971017, 51971018, 11921006, 11975034 and 12004010) and the Science Funds for Creative Research Groups of China (No. 51921001), Program for Changjiang Scholars and Innovative Research Team in University of China (No. IRT_14R05), National Magnetic Confinement Fusion Energy Research Project (2017YFE0302500, 2018YFE0307100 and 2019YFE03120003) from Ministry of Science and Technology of China, and Projects of SKLAMM-USTB (No. 2018Z-19). Dr. H. Wang acknowledges the financial support from the Fundamental Research Funds for the Central Universities of China (No. FRF-TP-18-004C1), E.F. appreciates the support from the Ion Beam Materials Laboratory (IBML) at Peking University.

References

- [1] J.W. Yeh, S.K. Chen, S.J. Lin, J.Y. Gan, T.S. Chin, T.T. Shun, C.H. Tsau, S.Y. Chang, Nanostructured high-entropy alloys with multiple principal elements: novel alloy design concepts and outcomes, *Adv. Eng. Mater.* 6 (2004) 299–303.
- [2] B. Cantor, K.B. Kim, P.J. Warren, Novel multicomponent amorphous alloys, *MSF* 386–388 (2002) 27–32.
- [3] Y.J. Zhou, Y. Zhang, Y.L. Wang, G.L. Chen, Two kinds of quantum adiabatic approximation, *Phys. Lett. A* 368 (2007) 18–24.
- [4] L.H. Wen, H.C. Kou, J.S. Li, H. Chang, X.Y. Xue, L. Zhou, Effect of aging temperature on microstructure and properties of AlCoCrCuFeNi high-entropy alloy, *Intermetallics* 17 (2009) 266–269.
- [5] O.N. Senkov, G.B. Wilks, J.M. Scott, D.B. Miracle, Mechanical properties of Nb₂₅Mo₂₅Ta₂₅W₂₅ and V₂₀Nb₂₀Mo₂₀Ta₂₀W₂₀ refractory high entropy alloys, *Intermetallics* 19 (2011) 698–706.
- [6] M.H. Chuang, M.H. Tsai, W.R. Wang, S.J. Lin, J.W. Yeh, Microstructure and wear behavior of Al_xCo_{1.5}Cr_{Fe}Ni_{1.5}Tiy high-entropy alloys, *Acta Mater.* 59 (2011) 6308–6317.
- [7] X.W. Qiu, Y.P. Zhang, L. He, C.G. Liu, Microstructure and corrosion resistance of AlCrFeCuCo high entropy alloy, *J. Alloy. Compd.* 549 (2013) 195–199.
- [8] Y.Y. Chen, T. Duval, U.D. Hung, J.W. Yeh, H.C. Shih, Microstructure and electrochemical properties of high entropy alloys—a comparison with type-304 stainless steel, *Corros. Sci.* 47 (2005) 2257–2279.
- [9] N.A.P.K. Kumar, C. Li, K.J. Leonard, H. Bei, S.J. Zinkle, Microstructural stability and mechanical behavior of FeNiMnCr high entropy alloy under ion irradiation, *Acta Mater.* 113 (2016) 230–244.
- [10] M.R. He, S. Wang, K. Jin, H. Bei, K. Yasuda, S. Matsumura, K. Higashida, I.M. Robertson, Enhanced damage resistance and novel defect structure of CrFeCoNi under in situ electron irradiation, *Scripta Mater.* 125 (2016) 5–9.
- [11] Y. Zhang, G.M. Stocks, K. Jin, C. Lu, H. Bei, B.C. Sales, L. Wang, L.K. Béland, R.E. Stoller, G.D. Samolyuk, M. Caro, A. Caro, W.J. Weber, Influence of chemical disorder on energy dissipation and defect evolution in concentrated solid solution alloys, *Nat. Commun.* 6 (2015) 8736.
- [12] C. Lu, L. Niu, N. Chen, K. Jin, T. Yang, P. Xiu, Y. Zhang, F. Gao, H. Bei, S. Shi, M.R. He, I.M. Robertson, W.J. Weber, L. Wang, Pleckstrin homology domain-containing protein PHLD3B supports cancer growth via a negative feedback loop involving p53, *Nat. Commun.* 7 (2016) 13755.
- [13] T. Egami, W. Guo, P.D. Rack, T. Nagase, Irradiation resistance of multicomponent alloys, *Metall. Mater. Trans. A* 45 (2014) 180–183.
- [14] T. Nagase, P.D. Rack, J.H. Noh, T. Egami, In-situ TEM observation of structural changes in nano-crystalline CoCrCuFeNi multicomponent high-entropy alloy (HEA) under fast electron irradiation by high voltage electron microscopy (HVEM), *Intermetallics* 59 (2015) 32–42.
- [15] D. Chen, Y. Tong, J. Wang, B. Han, Y.L. Zhao, F. He, J.J. Kai, Microstructural response of He+ irradiated FeCoNiCrTiO₂ high-entropy alloy, *J. Nucl. Mater.* 510 (2018) 187–192.
- [16] M.-R. He, S. Wang, S. Shi, K. Jin, H. Bei, K. Yasuda, S. Matsumura, K. Higashida, I.M. Robertson, Mechanisms of radiation-induced segregation in CrFeCoNi-based single-phase concentrated solid solution alloys, *Acta Mater.* 126 (2017) 182–193.
- [17] J.Y. He, H. Wang, H.L. Huang, X.D. Xu, M.W. Chen, Y. Wu, X.J. Liu, T.G. Nieh, K. An, Z.P. Lu, A precipitation-hardened high-entropy alloy with outstanding tensile properties, *Acta Mater.* 102 (2016) 187–196.
- [18] K. Ming, X. Bi, J. Wang, Precipitation strengthening of ductile Cr 15 Fe 20 Co 35 Ni 20 Mo 10 alloys, *Scr. Mater.* 137 (2017) 88–93.
- [19] B. Gwalani, V. Soni, M. Lee, S.A. Mantri, Y. Ren, R. Banerjee, Optimizing the coupled effects of Hall-Petch and precipitation strengthening in a Al 0.3 CoCrFeNi high entropy alloy, *Mater. Des.* 121 (2017) 254–260.
- [20] M. Laurent-Brocq, X. Sauvage, A. Akhatova, L. Perrière, E. Leroy, Y. Champion, Precipitation and hardness of carbonitrides in a CrMnFeCoNi high entropy alloy: precipitation of carbonitrides in HEA, *Adv. Eng. Mater.* 19 (2017) 1600715.
- [21] Y. Etoh, S. Shimada, Neutron irradiation effects on intermetallic precipitates in Zircaloy as a function of fluence, *J. Nucl. Mater.* 200 (1993) 59–69.
- [22] Z.W. Zhang, C.T. Liu, X.L. Wang, M.K. Miller, D. Ma, G. Chen, J.R. Williams, B.A. Chin, Effects of proton irradiation on nanocluster precipitation in ferritic steel containing fcc alloying additions, *Acta Mater.* 60 (2012) 3034–3046.
- [23] R.S. Nelson, J.A. Hudson, D.J. Mazey, The stability of precipitates in an irradiation environment, *J. Nucl. Mater.* 44 (1972) 318–330.
- [24] D.I. Potter, D.G. Ryding, Precipitate coarsening, redistribution and renucleation during irradiation of Ni-6.35 wt% Al, *J. Nucl. Mater.* 71 (1977) 14–24.
- [25] G. Yeli, D. Chen, K. Yabuuchi, A. Kimura, S. Liu, W. Lin, Y. Zhao, S. Zhao, J. Kai, The stability of γ' precipitates in a multi-component FeCoNiCrTiO₂ alloy under elevated-temperature irradiation, *J. Nucl. Mater.* 540 (2020) 152364.
- [26] T. Yang, W. Guo, J.D. Poplawsky, D. Li, L. Wang, Y. Li, W. Hu, M.L. Crespiello, Z. Yan, Y. Zhang, Y. Wang, S.J. Zinkle, Structural damage and phase stability of Al_{0.3}CoCrFeNi high entropy alloy under high temperature ion irradiation, *Acta Mater.* 188 (2020) 1–15.
- [27] R.E. Stoller, M.B. Toloczo, G.S. Was, A.G. Certain, S. Dwaraknath, F.A. Garner, On the use of SRIM for computing radiation damage exposure, *Nucl. Instrum. Methods Phys. Res. Sect. B Beam Interact. Mater. At.* 310 (2013) 75–80.
- [28] W.J. Weber, Y. Zhang, Predicting damage production in monoatomic and multi-elemental targets using stopping and range of ions in matter code: challenges and recommendations, *Curr. Opin. Solid State Mater. Sci.* 23 (2019) 100757.
- [29] G.J.C. Carpenter, E.M. Schulson, Effects of 1 MeV electron irradiation on Ni₃Al, *Scr. Metall.* 15 (1981) 549–554.
- [30] Y. Yang, C. Zhang, Y. Meng, J. Liu, J. Gou, Y. Xian, Y. Song, Nanoindentation on V-4Ti alloy irradiated by H and He ions, *J. Nucl. Mater.* 459 (2015) 1–4.
- [31] G.M. Pharr, E.G. Herbert, Y. Gao, The Indentation size effect: a critical examination of experimental observations and mechanistic interpretations, *Annu. Rev. Mater. Res.* 40 (2010) 271–292.
- [32] C. Heintze, F. Bergner, M. Hernández-Mayoral, Ion-irradiation-induced damage in Fe-Cr alloys characterized by nanoindentation, *J. Nucl. Mater.* 417 (2011) 980–983.
- [33] R. Kasada, Y. Takayama, K. Yabuuchi, A. Kimura, A new approach to evaluate irradiation hardening of ion-irradiated ferritic alloys by nano-indentation techniques, *Fusion Eng. Des.* 86 (2011) 2658–2661.
- [34] K. Yabuuchi, Y. Kurabayashi, S. Nogami, R. Kasada, A. Hasegawa, Evaluation of irradiation hardening of proton irradiated stainless steels by nanoindentation, *J. Nucl. Mater.* 446 (2014) 142–147.
- [35] F. Tuomisto, I. Makkonen, J. Heikinheimo, F. Granberg, F. Djurabekova, K. Nordlund, G. Velisa, H. Bei, H. Xue, W.J. Weber, Y. Zhang, Segregation of Ni at early stages of radiation damage in NiCoFeCr solid solution alloys, *Acta Mater.* 196 (2020) 44–51.

- [36] S. Abhaya, R. Rajaraman, S. Kalavathi, C. David, B.K. Panigrahi, G. Amarendra, Effect of dose and post irradiation annealing in Ni implanted high entropy alloy FeCrCoNi using slow positron beam, *J. Alloy. Compd.* 669 (2016) 117–122.
- [37] J. Qiu, Y. Xin, X. Ju, L.P. Guo, B.Y. Wang, Y.R. Zhong, Q.Y. Huang, Y.C. Wu, Investigation by slow positron beam of defects in CLAM steel induced by helium and hydrogen implantation, *Nucl. Instrum. Methods Phys. Res. Sect. B Beam Interact. Mater. At.* 267 (2009) 3162–3165.
- [38] X. Lian, X. Cao, Y. Zhao, S. Jin, J. Luo, T. Zhu, Y. Gong, B. Wang, R. Yu, *Phys. Status Solidi Appl. Mater. Sci.* 215 (2018) 1–6.
- [39] H. Huang, J. Gao, B. Radiguet, R. Liu, J. Li, G. Lei, Q. Huang, M. Liu, R. Xie, Microstructural evolution and hardening of GH3535 alloy under energetic Xe ion irradiation at room temperature and 650 °C, *J. Nucl. Mater.* 499 (2018) 431–439.
- [40] K. Jin, W. Guo, C. Lu, M.W. Ullah, Y. Zhang, W.J. Weber, L. Wang, J.D. Poplawsky, H. Bei, Effects of Fe concentration on the ion-irradiation induced defect evolution and hardening in Ni-Fe solid solution alloys, *Acta Mater.* 121 (2016) 365–373.
- [41] K.Y. Liou, P. Wilkes, The radiation disorder model of phase stability, *J. Nucl. Mater.* 87 (1979) 317–330.
- [42] F. Bourdeau, C. Abromeit, H. Wollenberger, Disordering and dissolution of γ' precipitates under ion irradiation, *Phys. Rev. B* 50 (1994) 16205–16211.
- [43] A. Ardell, Precipitation hardening, *MTA* 16 (1985) 2131–2165.
- [44] C. Sun, M. Kirk, M. Li, K. Hattar, Y. Wang, O. Anderoglu, J. Valdez, B.P. Uberuaga, R. Dickerson, S.A. Maloy, Microstructure, chemistry and mechanical properties of Ni-based superalloy Rene N4 under irradiation at room temperature, *Acta Mater.* 95 (2015) 357–365.
- [45] Z. Yao, M.L. Jenkins, M.A. Kirk, Z. Yao, M.L. Jenkins, M.A.K. Heavy-ion, Heavy-ion irradiations of Fe and Fe-Cr model alloys Part 1: damage evolution in thin-foils at lower doses, *Philos. Mag.* 88 (2008) 2851–2880.
- [46] M. Desormeaux, B. Rouxel, A.T. Motta, M. Kirk, C. Bisor, Y. De Carlan, A. Legris, Development of radiation damage during in-situ Kr++ irradiation of Fe Ni Cr model austenitic steels, *J. Nucl. Mater.* 475 (2016) 156–167.
- [47] Z. Fan, W. Zhong, K. Jin, H. Bei, Y.N. Osetsky, Y. Zhang, Diffusion-mediated chemical concentration variation and void evolution in ion-irradiated NiCoFeCr high-entropy alloy, *J. Mater. Res.* (2020) 1–13.
- [48] C. Hofer, E. Stergar, S.A. Maloy, Y.Q. Wang, P. Hosemann, An intermetallic forming steel under radiation for nuclear applications, *J. Nucl. Mater.* 458 (2015) 361–368.
- [49] A.P. Druzhkov, S.E. Danilov, D.A. Perminov, V.L. Arbuzov, Formation and evolution of intermetallic nanoparticles and vacancy defects under irradiation in Fe Ni Al ageing alloy characterized by resistivity measurements and positron annihilation, *J. Nucl. Mater.* 476 (2016) 168–178.
- [50] I.J. Beyerlein, M.J. Demkowicz, A. Misra, B.P. Uberuaga, Defect-interface interactions, *Prog. Mater. Sci.* 74 (2015) 125–210.